Matter

CellPress

Article

# Room temperature circularly polarized emission in perovskite nanocrystals through bichiral-molecule-induced lattice reconstruction

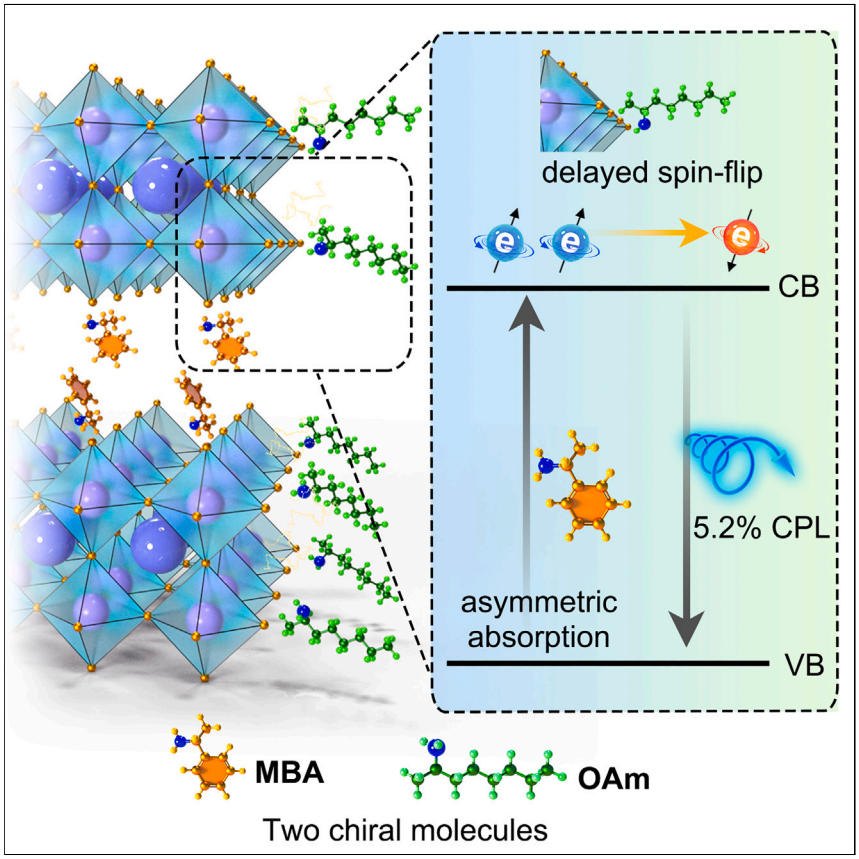


Chenlu He, Jian Qiu, Zhen Mu, ..., Xian Qin, Guichuan Xing, Xiaogang Liu

gcxing@um.edu.mo (G.X.)
chmlx@nus.edu.sg (X.L.)

## Highlights

Bichiral molecules collaborate to boost perovskite-based CPL

Degree of polarization up to 5.2% at room temperature with high thermal stability

Ultrafast spectroscopy reveals time-resolved spintronics

Bichiral perovskite nanoscintillators initiate asymmetric photopolymerization

By employing a chiral spacer in the crystal lattice and another chiral ligand on the surface of perovskite nanocrystals, we enhance asymmetric light absorption and delay the spin flip of photogenerated charge carriers. The coexistence of two types of chiral molecules in low-dimensional perovskite nanocrystals leads to a CPL signal at room temperature. We also demonstrate the use of these bichiral perovskite nanoscintillators to improve the reactivity and enantioselectivity of asymmetric photopolymerization under X-ray irradiation.

1 **Discovery**
A new material or phenomena

He et al., Matter 7, 475–484
February 7, 2024 
https://doi.org/10.1016/j.matt.2023.12.007

Matter

CellPress

Article

# Room temperature circularly polarized emission in perovskite nanocrystals through bichiral-molecule-induced lattice reconstruction

Chenlu He,[1,6] Jian Qiu,[1,2,6] Zhen Mu,[1,6] Jiaye Chen,[1] Yiming Wu,[3] Zhengzhi Jiang,[1] Pinzheng Zhang,[1] Xian Qin,[4] Guichuan Xing,[5,*] and Xiaogang Liu[1,2,3,7,*]

## SUMMARY

**Circularly polarized luminescence in halide organic-inorganic perovskite nanocrystals is attainable using chiral organic components. However, this phenomenon is typically restricted to cryogenic conditions due to exciton spin-flip processes. Here, we present a chiral-molecule-mediated lattice reconstruction method to induce circularly polarized luminescence in hybrid perovskite nanocrystals at room temperature. By employing a chiral spacer in the crystal lattice and another chiral ligand on the crystal surface, we enhance asymmetric light absorption and delay the spin flip of photogenerated charge carriers, as confirmed by circularly polarized pump-probe transient absorption spectroscopy. This cooperative interaction among chiral molecules results in circularly polarized emission with a polarization degree of 5.2% in mixed-phase perovskite nanocrystals. We demonstrate the application of chiral perovskites as nanoscintillators, where X-ray-induced asymmetric photopolymerization is achieved at room temperature through emitted circularly polarized radioluminescence. This property facilitates controlled *in situ* asymmetric photochemical reactions, fostering advancements in materials, drug delivery, and bioengineering applications.**

## INTRODUCTION

Halide organic-inorganic perovskites are promising alternatives to conventional semiconductors for a variety of applications, such as solar cells, lasers, light-emitting diodes, and photodetectors[1–4]. These materials offer several advantages, including high defect tolerance, solution processability, and ease of optoelectronic modulation.[5–10] Due to their predominantly ionic lattice and relatively soft crystal structure, halide perovskites can accommodate various dopants and organic molecules.[11] In particular, the generation of chiral perovskites by incorporating chiral organic molecules into the host scaffold has attracted considerable research interest, as the resulting chiral structures could serve as a source of circularly polarized luminescence (CPL) that facilitates the development of smart optoelectronics and spintronics.[12,13]

Chiral spacers, such as R/S-methylbenzylamine (R/S-MBA), are frequently employed to synthesize chiral perovskite films with intrinsic circular dichroism (CD). These spacers can impose symmetry constraints on the atomic geometry, resulting in chiral perovskite structures that exhibit unique CPL properties under cryogenic conditions.[14,15] To date, two-dimensional chiral perovskites have exhibited the highest degree of polarization (P = 17.6%) at 77 K.[16] In another study, a polarization of approximately 11% was observed for chiral perovskite films with low geometric

## PROGRESS AND POTENTIAL

Chiral perovskite nanocrystals are promising for optoelectronics and spintronics due to their circularly polarized luminescence (CPL). However, these materials often lose their CPL properties at room temperature. This work reports a simple method to create bichiral perovskite nanocrystals that maintain their CPL at room temperature. By combining chiral interior spacers and surface ligands, these nanocrystals develop a chiral structure that significantly enhances light absorption asymmetry. Moreover, the surface ligands can suppress the spin flip of the photogenerated charge carriers. The coexistence of large asymmetric light absorption (circular dichroism) and the inhibition of spin-flip of carriers contributes to a CPL signal with 5.2% circular polarization. These nanocrystals have the potential to enhance the enantioselectivity of asymmetric photopolymerization under X-ray irradiation.

dimensionality and a mixed-phase structure at 2 K in a 7 T magnetic field.[17] Despite the success, the CPL signal decreases significantly with increasing temperature, resulting in unpolarized emission at room temperature. This phenomenon is mainly attributed to the thermally activated spin flip of excitons, which occurs independently of the structural chirality of the perovskite lattice.[18] In this regard, it is vital to develop a simple and effective approach to suppress exciton spin flipping in chiral perovskites at room temperature.

CPL signals are usually obtained by introducing chiral ligands to nanocrystal surfaces.[19,20] This induces chirality transfer by coupling the static dipole of chiral ligands with the transition dipole moment of the nanocrystals.[21] Although the atomic structure of the core remains achiral, the chiral-ligand-induced electrical field on the surface regulates the electronic distribution and generates CPL.[22] For example, using chiral ligands, perovskite nanocrystals can achieve a room temperature circular polarization of 3.4%, attributable to the chiral-induced spin selectivity (CISS).[23] The temperature-stable CISS effect demonstrates the strong coupling between molecular chirality and electron spin, providing a promising technique to achieve CPL in achiral nanomaterials at room temperature.[24] Nevertheless, the intrinsic CD signal of perovskite nanocrystals is extremely weak, which makes it difficult to distinguish and utilize left- and right-handed photons.[25,26]

In this work, we demonstrate a facile and cost-effective synthesis of chiral perovskite nanocrystals of formamidinium lead bromide ($FAPbBr_3$) with room temperature CPL through the cooperation between chiral interior spacers and chiral surface ligands. The introduction of R/S-MBA spacers into nanocrystals creates chiral crystal lattices, resulting in greater asymmetric light absorption. Moreover, chiral R/S-2-octylamines (R/S-OAms) are employed as surface ligands to hinder the spin flip of excitons (Figure 1). The coexistence of large asymmetric absorption and suppressed spin flip leads to a CPL signal with 5.2% circular polarization, the highest ever observed in perovskite nanocrystals at room temperature.[27–30] We also demonstrate the use of these chiral perovskite nanoscintillators to improve the reactivity and enantioselectivity of asymmetric photopolymerization at room temperature under X-ray irradiation.

## RESULTS AND DISCUSSION

### Structural features of low-dimensional perovskite nanocrystals

In a typical experiment, we prepared low-dimensional $FAPbBr_3$ nanocrystals by intercalating molecular spacers ($MBA^+$ cations) between the planes of $[PbBr6]^{4-}$ octahedra. The presence of $MBA^+$ within $FAPbBr_3$ nanocrystals was confirmed by solid-state $^1H$ nuclear magnetic resonance (NMR) spectroscopy, as evidenced by the NMR signals at about 5.3 ppm, while undoped $FAPbBr_3$ showed signals above 6.0 ppm (Figures 2A and 2B).[31] It is noteworthy that protons on the chiral carbon of $MBA^+$ are responsible for the NMR signals of ~5.3 ppm in the MBA-doped sample. This MBA intercalation was further characterized by two-dimensional (2D) solid-state NMR spectroscopy (Figures 2C and S1). Moreover, the use of MBA resulted in the formation of large, low-dimensional mixed-phase nanocrystals, while undoped controls produced 3D monodisperse nanocubes of approximately 15 nm.[32,33] In addition, high-resolution transmission electron microscopy (HRTEM) was used to confirm the incorporation of $MBA^+$ into the perovskite lattice. In the case of the conventional 3D $FAPbBr_3$, the HRTEM image of a single particle showed a lattice spacing of 3.0 Å, which could be assigned to the (200) plane of cubic nanocrystals. In contrast, the MBA-doped low-dimensional nanocrystals exhibited an increased interplanar spacing of about 5.2 Å, which could be assigned to the n = 3 (200) plane.[34]

[1]Department of Chemistry, National University of Singapore, Singapore 117549, Singapore

[2]Joint School of National University of Singapore and Tianjin University, International Campus of Tianjin University, Binhai New City, Fuzhou 350207, China

[3]Institute of Materials Research and Engineering, Agency for Science, Technology and Research (A*STAR), Singapore 138634, Singapore

[4]Strait Institute of Flexible Electronics (SIFE Future Technologies), Fujian Normal University, Fuzhou 350117, China

[5]Joint Key Laboratory of the Ministry of Education, Institute of Applied Physics and Materials Engineering, University of Macau, Avenida da Universidade, Taipa, Macau 999078, China

[6]These authors contributed equally

[7]Lead contact

*Correspondence: gcxing@um.edu.mo (G.X.), chmlx@nus.edu.sg (X.L.)

https://doi.org/10.1016/j.matt.2023.12.007

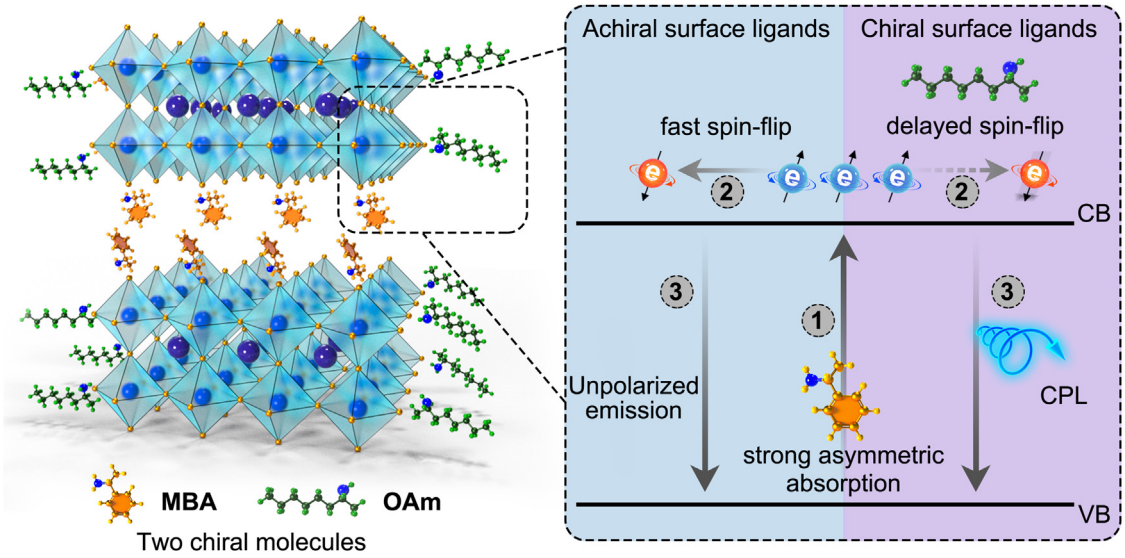


**Figure 1. Design of bichiral perovskite nanocrystals for room temperature CPL**

In our design, two types of chiral molecules are used to grow chiral perovskite nanocrystals: methylbenzylamine (MBA; in orange) spacers are inserted into nanocrystal lattices, while 2-octylamines (OAms; in green) molecules modify nanocrystal surfaces. Because of the cooperation between the two, asymmetric light absorption increases and exciton spin flipping is suppressed, contributing to enhanced room temperature CPL. CB, conduction band; VB, valence band.

X-ray diffraction (XRD) investigations of 3D $FAPbBr_3$ nanocrystals displayed characteristic diffraction peaks at 2θ of approximately 15° and 30°, corresponding to the (001) and (002) planes, respectively, of typical cubic nanocrystals (Figure 2E). However, MBA-doped nanocrystals exhibited diffraction peaks below 15°, which was consistent with layered crystal structures.[35] Furthermore, we constructed an MBA-intercalated $FAPbBr_3$ atomic supercell in which a bilayer MBA was inserted into the (001) planes of $[PbBr6]^{4-}$ octahedra, followed by structural optimization by first-principles calculations based on density functional theory (DFT). The intercalation of MBA increased the vertical distance between the $[PbBr6]^{4-}$ inorganic layers by ~87% (Figures 2D and S2; Table S1), which was close to the increase in the lattice spacing evidenced by XRD. The interaction between MBA and the inorganic frameworks was dominated by H−Br hydrogen bonding.[36] Moreover, the MBA intercalation induced a strong rotation of neighboring $FA^+$ molecules. These distinct differences in crystal structure and morphology confirmed the successful formation of low-dimensional nanocrystals using the MBA spacer.[37–39] The low-dimensional MBA-$FAPbBr_3$ displays enhanced quantum confinement, which effectively mitigates ion migration and the self-doping effect, consequently leading to improved intrinsic stability (Figures S3 and S4).

## Optical properties of bichiral perovskite nanocrystals

These MBA-doped low-dimensional nanocrystals showed a large band gap and multiple quantum well structures, similar to low-dimensional polycrystalline perovskite films (Figures 3A–3C).[40–42] The high miscibility of chiral MBA and OAm molecules allowed for the fabrication of four types of chiral nanocrystals with unique chiroptical signatures in CD spectroscopy: SS, SR, RS, and RR, where the first letter denotes the chiral configuration of the spacer MBA and the latter denotes the chiral configuration of the surface ligand OAm. Compared to the CD signals of MBA or OAm in the UV region, we observed characteristic bisignate CD signals of SS and RR nanocrystals at the corresponding absorption band in the UV-visible (UV-vis) region (Figures 3D and S5). The

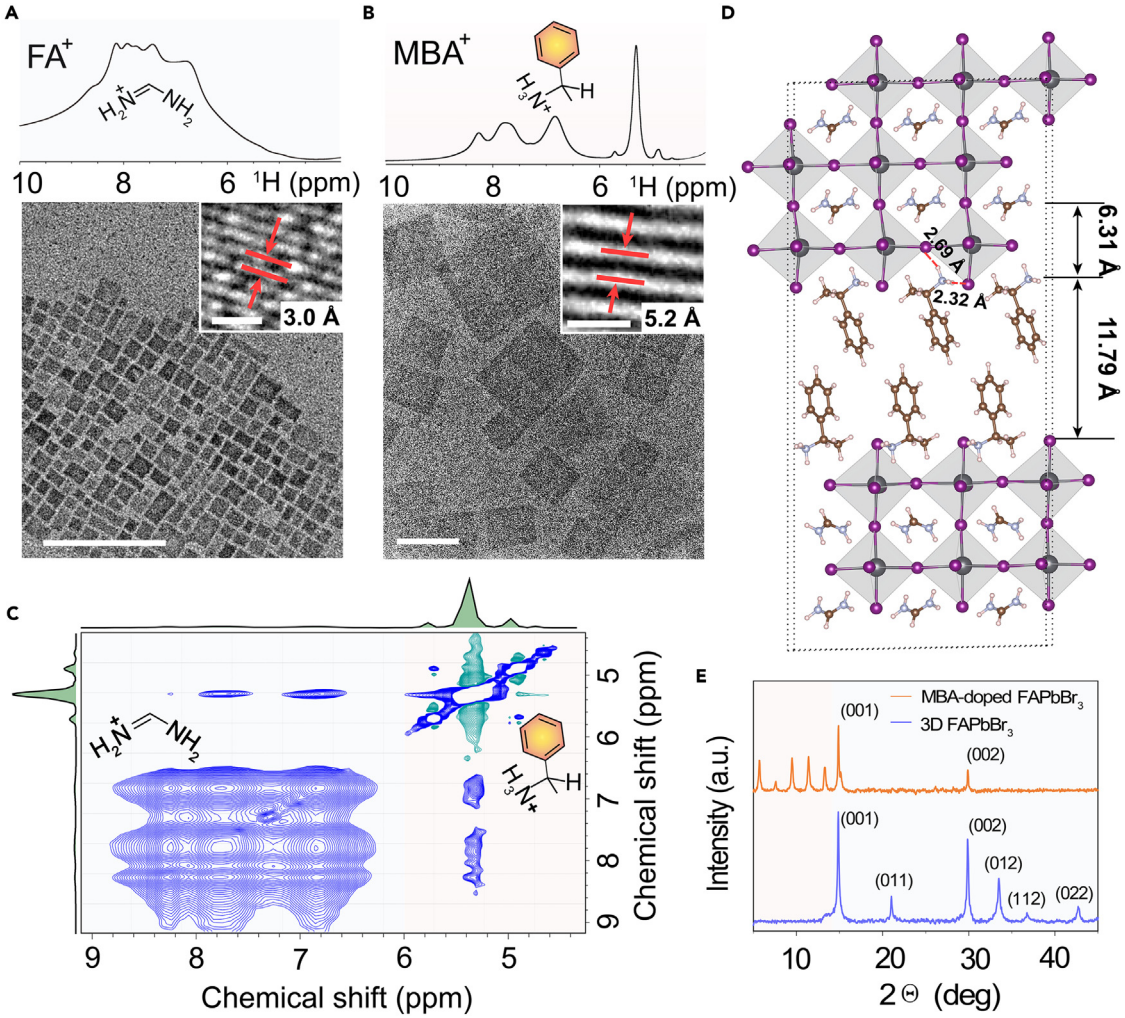


**Figure 2. Structural characterization of perovskite nanocrystals**

(A and B) $^{1}$H NMR spectra and TEM images of $FAPbBr_3$ and MBA-doped $FAPbBr_3$ nanocrystals, respectively. Scale bar: 100 nm. Insets are the corresponding HRTEM images. Scale bar: 1 nm.

(C) 2D solid-state NMR spectra of MBA-doped $FAPbBr_3$ nanocrystals. The $MBA^+/FA^+$ value is approximately 11% through analyzing the integrated area of the NMR peaks.

(D) Optimized atomic structure of MBA-doped $FAPbBr_3$. Purple, silver, brown, gray, and white balls denote bromide, lead, carbon, nitrogen, and hydrogen atoms, respectively.

(E) XRD patterns of MBA-doped and undoped $FAPbBr_3$ nanocrystals.

optical activity was likely induced by the chirality transfer from organic molecules to inorganic scaffolds. Specifically, the SS nanocrystals showed a positive Cotton effect with a maximum signal at ~465 nm and a crossover at ~354 nm. When RR nanocrystals were tested, the corresponding CD spectrum reversed signs due to the mirror symmetry of these two samples. In addition, the optical activity could be influenced by the cooperative interactions between the chiral MBA and OAm molecules, which can be quantified by the anisotropy factor $g_{abs}$.[43] SS or RR nanocrystals exhibited a high level of asymmetry, with a maximum $|g_{abs}|$ of about $2.0 \times 10^{-3}$, whereas the SR or RS nanocrystals displayed a weaker Cotton effect with a maximum $|g_{abs}|$ of about $0.5 \times 10^{-3}$. This observation suggests that the coexistence of two types of chiral organic molecules with identical chiral configurations enhances the nanocrystal's intrinsic chirality, essential for achieving a high degree of polarization in CPL.

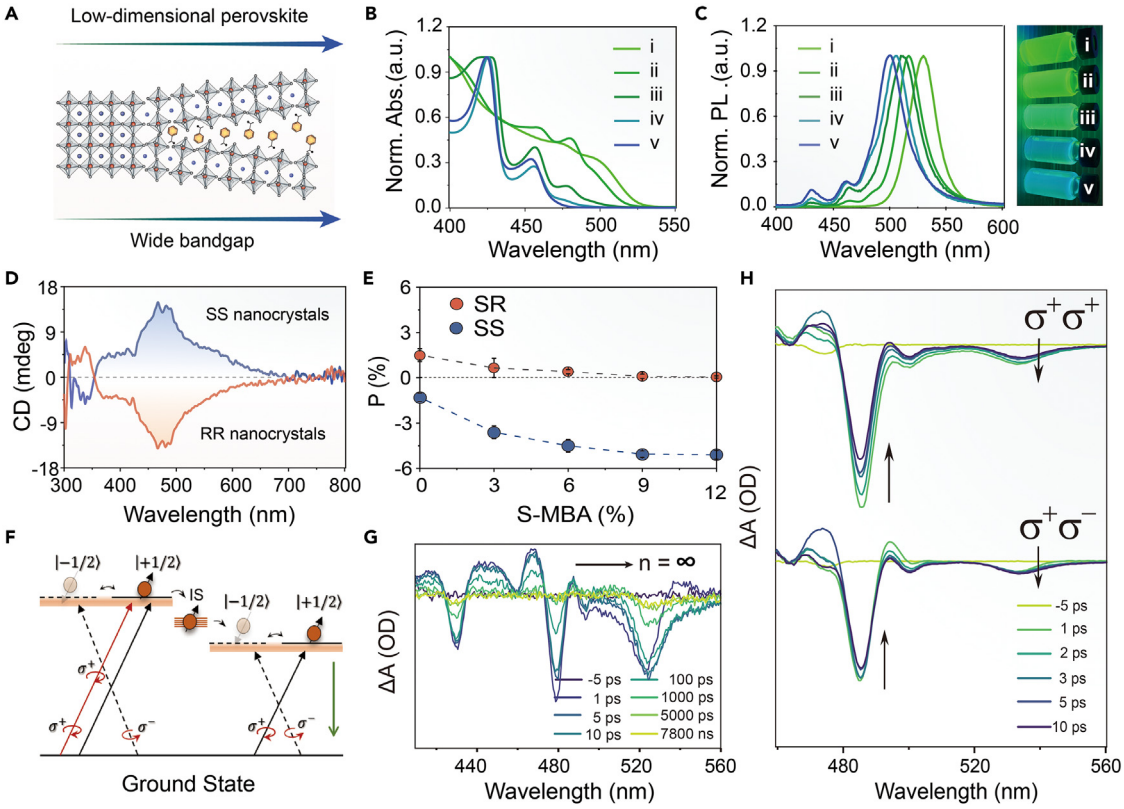


**Figure 3. Optical characterizations of bichiral perovskite nanocrystals**

(A) Schematic showing a dimensional reduction from 3D to low dimensions through MBA doping.

(B and C) Photoluminescence ($\lambda_{ex}$ = 365 nm) and UV-vis spectra of nanocrystals with MBA at various concentrations: (i–v) 0%, 3%, 6%, 9%, and 12%, respectively. Right: corresponding photograph of nanocrystals under 365 nm excitation.

(D) CD spectra of SS and RR nanocrystals.

(E) Degrees of polarization of SR and SS nanocrystals with various S-MBA doping contents. Error bars are defined as standard deviations of n = 3 independent measurements.

(F) Illustration of spin transfer in MBA-doped perovskite nanocrystals. IS, intermediate state.

(G) Transient absorption spectra of MBA-doped mixed-phase perovskite nanocrystals (pumped at 400 nm).

(H) Circularly polarized pump-probe transient absorption spectra of RR perovskite nanocrystals (pumped at 475 nm).

We next investigated the characteristics of CPL in SS and SR nanocrystals at room temperature. Using a linearly polarized 405 nm laser, we recorded polarization-resolved photoluminescence spectra of nanocrystals with different proportions of S-MBA molecules (Figures S6–S8).[16] We found that 3D nanocrystals modified only with R-OAm or S-OAm molecules generated left-handed or right-handed CPL with an averaged |P| value of ~1% at room temperature. Notably, the addition of S-MBA resulted in a contrasting maximum |P| value of 5.2% for SS nanocrystals, while their SR counterparts showed a |P| value of 0 (Figure 3E). These results suggest that the enhanced asymmetric light absorption and the suppressed exciton spin flipping contribute to CPL.

The dynamics of photogenerated charge carriers in the MBA-doped nanocrystals was investigated by transient absorption (TA) spectroscopy at room temperature, revealing a distinct energy transfer process from the low-dimensional to the high-dimensional phase (Figure 3G).[44] The RR perovskite nanocrystals exhibited two bleaching peaks at 485 (PB1) and 530 nm (PB2), corresponding to the low-dimensional phase (n = 3) and the 3D phase (n = ∞), respectively.[45] We further examined

spin transfer using circularly polarized pump-probe TA (CP-TA) spectroscopy (Figures 3F and 3H).[46–48] The upper curve was recorded under a right-handed circularly polarized pump with a right-handed circularly polarized probe ($\sigma^+\sigma^+$), while the lower curve was obtained using a right-handed circularly polarized pump with a left-handed circularly polarized probe ($\sigma^+\sigma^-$). In the case of $\sigma^+\sigma^+$, the bleaching peaks at 485 nm exhibited a rapid rise within 5 ps, which can be attributed to the selective excitation of spin-up electrons by the pump $\sigma^+$. This resulted in a non-equilibrium population of spin-up and spin-down electrons in the excited state. The excess spin-up electrons subsequently underwent spin relaxation by which the spin direction of the electrons flipped downward and an equilibrium spin population was reached. In contrast, the lower curve recorded under the $\sigma^+\sigma^-$ conditions characterized the inverse process, where rapid state filling occurred, as evidenced by a negative upward signal within the initial 5 ps. This ultrafast spin relaxation characteristic was observed in both RR and RS perovskite nanocrystals at PB1 and PB2 bleaching peaks (Figure S9). Lifetime fitting revealed that the spin relaxation occurred on a longer timescale (~3.0 ps) than energy transfer (~0.3 ps) from low- to high-dimensional phases, supporting the possibility of simultaneous spin transfer and energy transfer during rapid charge carrier formation in mixed-phase perovskite nanocrystals (Figure S10).

Next, we investigated the spin coherence of charge carriers in chiral OAm-modified perovskite nanocrystals at room temperature. By applying polarized pumping with polarized probes ($\sigma^+\sigma^+$ and $\sigma^+\sigma^-$), the OAm-modified nanocrystals showed distinct carrier dynamics near the exciton bleaching peak, indicating ligand-modulated spin relaxation of charge carriers (Figure 4A). Moreover, power-dependent experiments indicate that nanocrystals modified with chiral OAm have a longer spin relaxation time than those modified with achiral OAm (Figures 4B and S11). The spin lifetime of nanocrystals modified with achiral OAm decreased gradually from ~2 to ~0.8 ps with increasing carrier density, which is consistent with previous reports.[24] In contrast, the spin lifetime of nanocrystals modified with chiral OAm also decreased with carrier density but remained longer (~3–1.6 ps) than that of their counterparts modified with achiral OAm, suggesting that the suppressed spin flip was attributed to surface chiral ligands through CISS.

## Asymmetric photopolymerization triggered by bichiral perovskite nanoscintillators

The CPL of bichiral perovskite nanocrystals has the potential to induce asymmetric photopolymerization of achiral diacetylene monomers under X-ray irradiation at room temperature. The diacetylene monomer in the solid state showed an intense absorption below 200 nm (Figure S12), indicating that photopolymerization could be initiated by X-rays to generate conjugated polydiacetylene. However, X-rays alone cannot induce CPL-responsive asymmetric photopolymerization, as this requires specific waveplates that can convert X-rays into circularly polarized light, which presents a significant manufacturing challenge. To overcome this issue, bichiral perovskite nanocrystals synthesized with two types of chiral molecules can be used as chiral scintillators to emit circularly polarized radioluminescence upon X-ray irradiation.

The photopolymerization was carried out by exposing a hybrid film of diacetylene monomers with bichiral perovskite nanoscintillators (yellow film in Figure 4C) over an X-ray source. This film turned blue with intense absorption maximums at about 650 nm, thus confirming the formation of polydiacetylene.[43] With the use of chiral SS scintillators as the structural symmetry breaker, the resulting hybrid

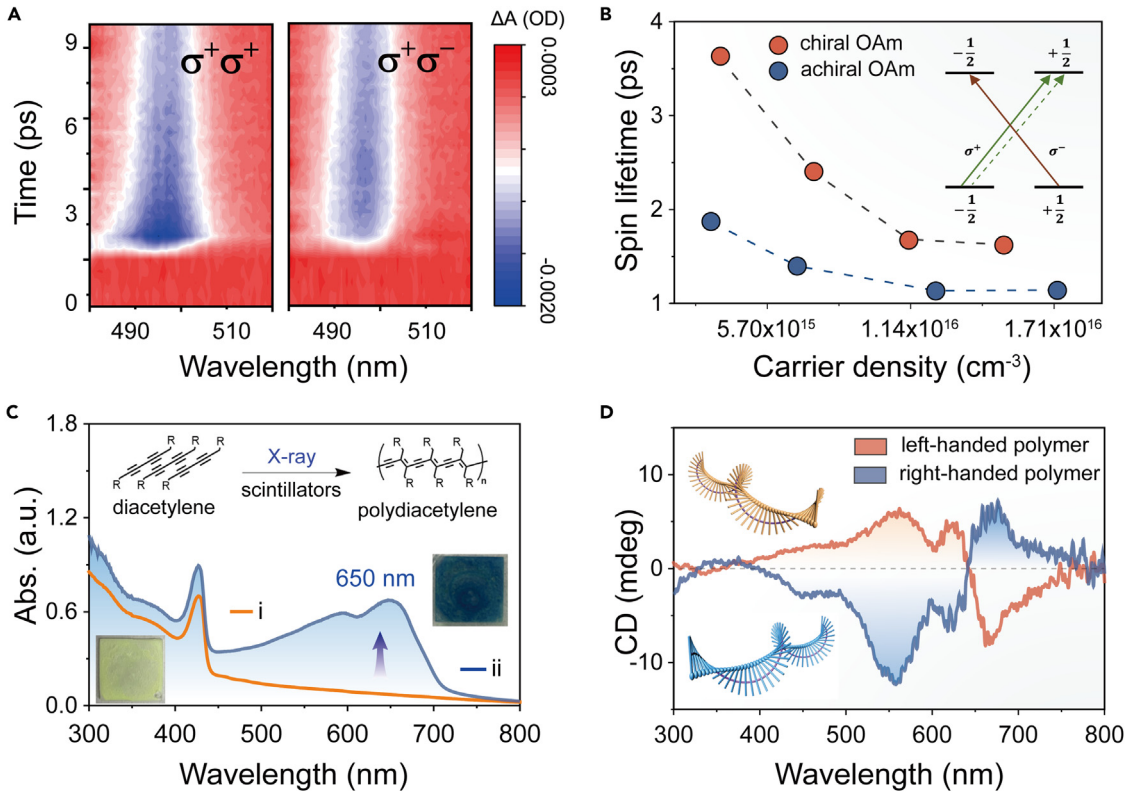


**Figure 4. Spin dynamics and asymmetric photopolymerization of perovskite nanocrystals**

(A) Spin dynamics of charge carriers in nanocrystals modified with chiral OAm ligands under $\sigma^+$ pump and $\sigma^+$ probe and under $\sigma^+$ pump and $\sigma^-$ probe.

(B) Power-dependent spin-coherence lifetime of nanocrystals modified with chiral OAm or achiral OAm ligands. Inset is the mechanistic illustration of spin-coherence lifetime measurement. The probe $\sigma^+$ selectively detects the change in spin polarization. The flip of a spin would simultaneously lead to a decay of the $\sigma^+$ bleach and a formation of the $\sigma^-$ bleach.

(C) UV-vis spectra and illustration of solid-state photopolymerization of diacetylene monomer under X-ray irradiation assisted with bichiral perovskite nanoscintillators. The insets show the hybrid film (i) before and (ii) after photopolymerization.

(D) CD spectra and illustration of left- and right-handed polydiacetylenes induced by chiral RR and SS perovskite nanoscintillators. The insets depict left- and right-handed polydiacetylene chains.

polydiacetylene films showed a right-handed polymer configuration and exhibited optical activity, as proven by the positive Cotton effect (Figure 4D). If chiral RR scintillators were used instead, the corresponding CD spectrum of resulting polydiacetylene flipped signs, indicating a predominantly left-handed polymer configuration. These results demonstrated that bichiral nanoscintillators can induce asymmetric photopolymerization under X-ray initiation, where the helical behavior of polydiacetylene chains was regulated by the CPL feature of chiral nanoscintillators. To further support this conclusion, two control experiments were performed. Firstly, polydiacetylene induced by RS and SR nanocrystals showed no chiral preference. Secondly, chiral organic molecules (MBA and OAm) were unable to generate chiral polydiacetylene under X-ray irradiation (Figure S13). Therefore, the successful break of structure symmetry in this photopolymerization can be attributed to the highly circular polarized emission from chiral nanoscintillators, which could improve the reactivity and enantioselectivity of photopolymerization (Figure S14). Moreover, by taking advantage of the very deep penetration of X-rays, asymmetric photopolymerization was achieved through materials that are challenging to penetrate with conventional UV or visible light, such as wood, polypropylene, and pig skin tissue. The resulting polymer exhibited similar CD signals with various intensities, indicating the

successful formation of chiral polydiacetylene (Figure S15). These results reveal the potential of chiral perovskite nanoscintillators to assist in X-ray-initiated asymmetric photopolymerization under challenging conditions.

### Conclusions

We outlined a feasible and economical protocol to produce chiral perovskite nanocrystals with high circularly polarized emission (P = 5.2%) at room temperature. The synergistic effect resulting from chiral OAm and MBA molecules functionalized in the nanocrystals leads to enhanced asymmetric light absorption and suppressed spin flip. Additionally, these bichiral perovskite scintillators were deployed as tools to induce asymmetric photopolymerization under X-ray. These findings open up new avenues for applications, in particular *in situ* asymmetric photochemical reactions within internal conditions or biological systems.

## EXPERIMENTAL PROCEDURES

### Resource availability

#### *Lead contact*

Further information and requests for resources should be directed to and will be fulfilled by the lead contact, Professor Xiaogang Liu (chmlx@nus.edu.sg).

#### *Materials availability*

Formamidinium acetate (FA-acetate; 99%), oleic acid (technical grade 90%), oleylamine (technical grade 70%), 1-octadecene (technical grade 90%), hexane (reagent grade ≥95%), R-MBA (98% purity), S-MBA (98% purity), and acetic acid (99% purity) were purchased from Sigma-Aldrich. Compound 10,12-pentacosadiynoic acid was purchased from Sigma-Aldrich and purified by being dissolved in hexane, followed by filtration to remove the polymer before use. R-OAm (98% purity) and (S)-2-octylamine (S-OAm; 98% purity) were purchased from Alfa Aesar.

#### *Data and code availability*

All relevant data that support the findings of this work are available from the corresponding author upon reasonable request.

## CHARACTERIZATIONS

All UV-vis spectra were recorded using an Agilent Cary 3500 spectrophotometer. Photoluminescence was recorded using a fluorescence spectrometer (FLSP920; Edinburgh Instruments, Livingston, UK) equipped with an Xe lamp. Powder XRD patterns were tested using a Bruker D8 Advance diffractometer with graphite-monochromatized CuKα radiation (λ = 0.15406 nm). TEM images were acquired using a JEOL JEM-3011 transmission electron microscope operated at 300 kV. HRTEM images were filtered using the ABSF Filter (average background subtracted filter) implemented by Digital Micrograph. CD spectra were measured using a JASCO CD J-815 spectrometer.

## SUPPLEMENTAL INFORMATION

Supplemental information can be found online at https://doi.org/10.1016/j.matt.2023.12.007.

## ACKNOWLEDGMENTS

This research was primarily funded through the National Research Foundation, the Prime Minister's Office of Singapore under its Competitive Research Program (CRP award no. NRF-CRP23-2019-0002), the NRF Investigatorship Programme

(award no.NRF-NRFI05-2019-0003), the Science and Technology Development Fund, Macao SAR (file nos.0082/2021/A2 and 006/2022/ALC), UM's research fund (file nos. MYRG2022-00241-IAPME and MYRG-CRG2022-00009-FHS), and the Natural Science Foundation of China (61935017 and 62175268).

## AUTHOR CONTRIBUTIONS

C.H. and J.Q. prepared the samples. Z.M. and Z.J. performed optical measurements. X.Q. performed DFT calculations. J.C. and P.Z. were responsible for TEM characterizations. X.L. and G.X. conceived the experiment and managed the research. X.Q., Y.W., G.X., and X.L. analyzed and discussed the results and wrote the manuscript.

## DECLARATION OF INTERESTS

The authors declare no competing interests.

Received: September 16, 2023
Revised: November 16, 2023
Accepted: December 6, 2023
Published: January 11, 2024

## REFERENCES

1. Xiang, W., and Tress, W. (2019). Review on recent progress of all-inorganic metal halide perovskites and solar cells. Adv. Mater. *31*, 1902851.

2. Qin, C., Sandanayaka, A.S.D., Zhao, C., Matsushima, T., Zhang, D., Fujihara, T., and Adachi, C. (2020). Stable room-temperature continuous-wave lasing in quasi-2D perovskite films. Nature *585*, 53–57.

3. Han, D., Imran, M., Zhang, M., Chang, S., Wu, X.G., Zhang, X., Tang, J., Wang, M., Ali, S., Li, X., et al. (2018). Efficient light-emitting diodes based on in situ fabricated FAPbBr3 nanocrystals: the enhancing role of the ligand-assisted reprecipitation process. ACS Nano *12*, 8808–8816.

4. Dong, Y., Zhang, Y., Li, X., Feng, Y., Zhang, H., and Xu, J. (2019). Chiral perovskites: promising materials toward next-generation optoelectronics. Small *15*, 1902237.

5. Akkerman, Q.A., Rainò, G., Kovalenko, M.V., and Manna, L. (2018). Genesis, challenges and opportunities for colloidal lead halide perovskite nanocrystals. Nat. Mater. *17*, 394–405.

6. Shamsi, J., Urban, A.S., Imran, M., De Trizio, L., and Manna, L. (2019). Metal halide perovskite nanocrystals: synthesis, post-synthesis modifications, and their optical properties. Chem. Rev. *119*, 3296–3348.

7. Almeida, G., Goldoni, L., Akkerman, Q., Dang, Z., Khan, A.H., Marras, S., Moreels, I., and Manna, L. (2018). Role of acid–base equilibria in the size, shape, and phase control of cesium lead bromide nanocrystals. ACS Nano *12*, 1704–1711.

8. Wang, H., Ye, F., Sun, J., Wang, Z., Zhang, C., Qian, J., Zhang, X., Choy, W.C.H., Sun, X.W., Wang, K., and Zhao, W. (2022). Efficient CsPbBr3 nanoplatelet-based blue light-emitting diodes enabled by engineered surface ligands. ACS Energy Lett. *7*, 1137–1145.

9. Dong, Y., Qiao, T., Kim, D., Parobek, D., Rossi, D., and Son, D.H. (2018). Precise control of quantum confinement in cesium lead halide perovskite quantum dots via thermodynamic equilibrium. Nano Lett. *18*, 3716–3722.

10. Bohn, B.J., Tong, Y., Gramlich, M., Lai, M.L., Döblinger, M., Wang, K., Hoye, R.L.Z., Müller-Buschbaum, P., Stranks, S.D., Urban, A.S., et al. (2018). Boosting tunable blue luminescence of halide perovskite nanoplatelets through postsynthetic surface trap repair. Nano Lett. *18*, 5231–5238.

11. Long, G., Sabatini, R., Saidaminov, M.I., Lakhwani, G., Rasmita, A., Liu, X., Sargent, E.H., and Gao, W. (2020). Chiral-perovskite optoelectronics. Nat. Rev. Mater. *5*, 423–439.

12. Wei, Q., and Ning, Z. (2021). Chiral perovskite spin-optoelectronics and spintronics: toward judicious design and application. ACS Mater. Lett. *3*, 1266–1275.

13. Ma, S., Ahn, J., and Moon, J. (2021). Chiral perovskites for next-generation photonics: from chirality transfer to chiroptical activity. Adv. Mater. *33*, 2005760.

14. Ahn, J., Lee, E., Tan, J., Yang, W., Kim, B., and Moon, J. (2017). A new class of chiral semiconductors: chiral-organic-molecule-incorporating organic–inorganic hybrid perovskites. Mater. Horiz. *4*, 851–856.

15. Lu, H., Xiao, C., Song, R., Li, T., Maughan, A.E., Levin, A., Brunecky, R., Berry, J.J., Mitzi, D.B., Blum, V., and Beard, M.C. (2020). Highly distorted chiral two-dimensional tin iodide perovskites for spin polarized charge transport. J. Am. Chem. Soc. *142*, 13030–13040.

16. Ma, J., Fang, C., Chen, C., Jin, L., Wang, J., Wang, S., Tang, J., and Li, D. (2019). Chiral 2D perovskites with a high degree of circularly polarized photoluminescence. ACS Nano *13*, 3659–3665.

17. Long, G., Jiang, C., Sabatini, R., Yang, Z., Wei, M., Quan, L.N., Liang, Q., Rasmita, A., Askerka, M., Walters, G., et al. (2018). Spin control in reduced-dimensional chiral perovskites. Nat. Photonics *12*, 528–533.

18. Chen, Y., Ma, J., Liu, Z., Li, J., Duan, X., and Li, D. (2020). Manipulation of valley pseudospin by selective spin injection in chiral two-dimensional perovskite/monolayer transition metal dichalcogenide heterostructures. ACS Nano *14*, 15154–15160.

19. Xu, L., Wang, X., Wang, W., Sun, M., Choi, W.J., Kim, J.Y., Hao, C., Li, S., Qu, A., Lu, M., et al. (2022). Enantiomer-dependent immunological response to chiral nanoparticles. Nature *601*, 366–373.

20. Sujith, M., Vishnu, E.K., Sappati, S., Oliyantakath Hassan, M.S., Vijayan, V., and Thomas, K.G. (2022). Ligand-induced ground- and excited-state chirality in silicon nanoparticles: surface interactions matter. J. Am. Chem. Soc. *144*, 5074–5086.

21. Forde, A., Ghosh, D., Kilin, D., Evans, A.C., Tretiak, S., and Neukirch, A.J. (2022). Induced chirality in halide perovskite clusters through surface chemistry. J. Phys. Chem. Lett. *13*, 686–693.

22. Ma, W., Xu, L., de Moura, A.F., Wu, X., Kuang, H., Xu, C., and Kotov, N.A. (2017). Chiral inorganic nanostructures. Chem. Rev. *117*, 8041–8093.

23. Kim, Y.-H., Zhai, Y., Gaulding, E.A., Habisreutinger, S.N., Moot, T., Rosales, B.A., Lu, H., Hazarika, A., Brunecky, R., Wheeler, L.M., et al. (2020). Strategies to achieve high circularly polarized luminescence from colloidal organic–inorganic hybrid perovskite nanocrystals. ACS Nano *14*, 8816–8825.

24. Kim, Y.-H., Zhai, Y., Lu, H., Pan, X., Xiao, C., Gaulding, E.A., Harvey, S.P., Berry, J.J., Vardeny, Z.V., Luther, J.M., and Beard, M.C. (2021). Chiral-induced spin selectivity enables a room-temperature spin light-emitting diode. Science *371*, 1129–1133.

25. Crassous, J., Fuchter, M.J., Freedman, D.E., Kotov, N.A., Moon, J., Beard, M.C., and Feldmann, S. (2023). Materials for chiral light control. Nat. Rev. Mater. *8*, 365–371.

26. Naaman, R., Paltiel, Y., and Waldeck, D.H. (2019). Chiral molecules and the electron spin. Nat. Rev. Chem *3*, 250–260.

27. Gao, J.X., Zhang, W.Y., Wu, Z.G., Zheng, Y.X., and Fu, D.W. (2020). Enantiomorphic perovskite ferroelectrics with circularly polarized luminescence. J. Am. Chem. Soc. *142*, 4756–4761.

28. Liu, Y., Luo, Z., Wei, Y., C, Li, C, Li, Y, Chen, X, He, X, Chang, and Z, Quan (2023). Integrating achiral and chiral organic ligands in zero-dimensional hybrid metal halides to boost circularly polarized luminescence. Angew. Chem. Int. Ed. *135*, e202306821.

29. Jin, K.H., Zhang, Y., Li, K.J., Sun, M.E., Dong, X.Y., Wang, Q.L., and Zang, S.Q. (2022). Enantiomorphic single crystals of linear lead (II) bromide perovskitoids with white circularly polarized emission. Angew. Chem. Int. Ed. *61*, e202205317.

30. Liu, D.Y., Li, H.Y., Han, R.P., Liu, H.L., and Zang, S.Q. (2023). Multiple stimuli-responsive luminescent chiral hybrid antimony chlorides for anti-counterfeiting and encryption applications. Angew. Chem. Int. Ed. *62*, e202307875.

31. Lu, H., Liu, Y., Ahlawat, P., Mishra, A., Tress, W.R., Eickemeyer, F.T., Yang, Y., Fu, F., Wang, Z., Avalos, C.E., et al. (2020). Vapor-assisted deposition of highly efficient, stable black-phase $FAPbI_3$ perovskite solar cells. Science *370*, eabb8985.

32. Wang, H., Xu, W., Wei, Q., Peng, S., Shang, Y., Jiang, X., Yu, D., Wang, K., Pu, R., Zhao, C., et al. (2023). In-situ growth of low-dimensional perovskite-based insular nanocrystals for highly efficient light emitting diodes. Light Sci. Appl. *12*, 62.

33. Xu, W., Ji, R., Liu, P., Cheng, L., Zhu, L., Zhang, J., Chen, H., Tong, Y., Zhang, C., Kuang, Z., et al. (2020). In situ-fabricated perovskite nanocrystals for deep-blue light-emitting diodes. J. Phys. Chem. Lett. *11*, 10348–10353.

34. Xu, Z., Lu, D., Liu, F., Lai, H., Wan, X., Zhang, X., Liu, Y., and Chen, Y. (2020). Phase distribution and carrier dynamics in multiple-ring aromatic spacer-based two-dimensional Ruddlesden–Popper perovskite solar cells. ACS Nano *14*, 4871–4881.

35. Liang, C., Gu, H., Xia, Y., Wang, Z., Liu, X., Xia, J., Zuo, S., Hu, Y., Gao, X., Hui, W., et al. (2020). Two-dimensional Ruddlesden–Popper layered perovskite solar cells based on phase-pure thin films. Nat. Energy *6*, 38–45.

36. Ma, S., Jung, Y.K., Ahn, J., Kyhm, J., Tan, J., Lee, H., Jang, G., Lee, C.U., Walsh, A., and Moon, J. (2022). Elucidating the origin of chiroptical activity in chiral 2D perovskites through nano-confined growth. Nat. Commun. *13*, 3259.

37. Cao, D.H., Stoumpos, C.C., Yokoyama, T., Logsdon, J.L., Song, T.B., Farha, O.K., Wasielewski, M.R., Hupp, J.T., and Kanatzidis, M.G. (2017). Thin films and solar cells based on semiconducting two-dimensional ruddlesden–popper $(CH_3(CH_2)_3NH_3)_2(CH_3NH_3)_{n-1}Sn_nI_{3n+1}$ perovskites. ACS Energy Lett. *2*, 982–990.

38. Yu, Y., Zhang, D., and Yang, P. (2017). Ruddlesden–Popper phase in two-dimensional inorganic halide perovskites: a plausible model and the supporting observations. Nano Lett. *17*, 5489–5494.

39. Deng, W., Jin, X., Lv, Y., Zhang, X., Zhang, X., and Jie, J. (2019). 2D Ruddlesden–Popper perovskite nanoplate based deep-blue light-emitting diodes for light communication. Adv. Funct. Mater. *29*, 1903861.

40. Liao, Y., Liu, H., Zhou, W., Yang, D., Shang, Y., Shi, Z., Li, B., Jiang, X., Zhang, L., Quan, L.N., et al. (2017). Highly oriented low-dimensional tin halide perovskites with enhanced stability and photovoltaic performance. J. Am. Chem. Soc. *139*, 6693–6699.

41. Liu, J., Leng, J., Wu, K., Zhang, J., and Jin, S. (2017). Observation of internal photoinduced electron and hole separation in hybrid two-dimensional perovskite films. J. Am. Chem. Soc. *139*, 1432–1435.

42. Zhou, N., Shen, Y., Li, L., Tan, S., Liu, N., Zheng, G., Chen, Q., and Zhou, H. (2018). Exploration of crystallization kinetics in quasi two-dimensional perovskite and high performance solar cells. J. Am. Chem. Soc. *140*, 459–465.

43. He, C., Feng, Z., Shan, S., Wang, M., Chen, X., and Zou, G. (2020). Highly enantioselective photo-polymerization enhanced by chiral nanoparticles and in situ photopatterning of chirality. Nat. Commun. *11*, 1188.

44. Chen, X., Lu, H., Wang, K., Zhai, Y., Lunin, V., Sercel, P.C., and Beard, M.C. (2021). Tuning spin-polarized lifetime in two-dimensional metal-halide perovskite through exciton binding energy. J. Am. Chem. Soc. *143*, 19438–19445.

45. Giovanni, D., Lim, J.W.M., Yuan, Z., Lim, S.S., Righetto, M., Qing, J., Zhang, Q., Dewi, H.A., Gao, F., Mhaisalkar, S.G., et al. (2019). Ultrafast long-range spin-funneling in solution-processed Ruddlesden-Popper halide perovskites. Nat. Commun. *10*, 3456.

46. Giovanni, D., Ma, H., Chua, J., Grätzel, M., Ramesh, R., Mhaisalkar, S., Mathews, N., and Sum, T.C. (2015). Highly spin-polarized carrier dynamics and ultralarge photoinduced magnetization in $CH_3NH_3PbI_3$ perovskite thin films. Nano Lett. *15*, 1553–1558.

47. Lin, X., Han, Y., Zhu, J., and Wu, K. (2023). Room-temperature coherent optical manipulation of hole spins in solution-grown perovskite quantum dots. Nat. Nanotechnol. *18*, 124–130.

48. Liu, S., Kepenekian, M., Bodnar, S., Feldmann, S., Heindl, M.W., Fehn, N., Zerhoch, J., Shcherbakov, A., Pöthig, A., Li, Y., et al. (2023). Bright circularly polarized photoluminescence in chiral layered hybrid lead-halide perovskites. Sci. Adv. *9*, eadh5083.

**Matter, Volume *7***

## Supplemental information

# Room temperature circularly polarized emission in perovskite nanocrystals through bichiral-molecule-induced lattice reconstruction

**Chenlu He, Jian Qiu, Zhen Mu, Jiaye Chen, Yiming Wu, Zhengzhi Jiang, Pinzheng Zhang, Xian Qin, Guichuan Xing, and Xiaogang Liu**

# Supporting Information

## Room-temperature circularly polarized emission in perovskite nanocrystals through bichiral molecular synchronization

Chenlu He[1], Jian Qiu[1,2], Zhen Mu[1], Jiaye Chen[1], Yiming Wu[3], Zhengzhi Jiang[1], Pinzheng Zhang[1], Xian Qin[4], Guichuan Xing[5*], and Xiaogang Liu[1,2,3*]

[1]Department of Chemistry, National University of Singapore, Singapore 117549, Singapore.

[2]Joint School of National University of Singapore and Tianjin University, International Campus of Tianjin University, Binhai New City, Fuzhou 350207, China.

[3]Institute of Materials Research and Engineering, Agency for Science, Technology and Research (A*STAR), Singapore, 138634, Singapore.

[4]Strait Institute of Flexible Electronics (SIFE Future Technologies), Fujian Normal University, Fuzhou 350117, China.

[5]Joint Key Laboratory of the Ministry of Education, Institute of Applied Physics and Materials Engineering, University of Macau, Avenida da Universidade, Taipa, Macau 999078, China.

*Corresponding author. E-mail: chmlx@nus.edu.sg (X. Liu.); gcxing@um.edu.mo (G. Xing)

**Table of contents** **pages**

**Materials and Methods**

Materials

Formamidinium acetate (FA-acetate, 99%), oleic acid (technical grade 90%), oleylamine (technical grade 70%), 1-octadecene (technical grade 90%), hexane (reagent grade ≥95%), R-methybenzylamine (R-MBA, 98% purity), S-methybenzylamine (S-MBA, 98% purity) and acetic acid (99% purity) were purchased from Sigma-Aldrich. Compound 10,12-pentacosadiynoic acid was purchased from Sigma-Aldrich and purified by dissolving in hexane, followed by filtration to remove the polymer before use. (R)-2-octylamine (R-OAm, 98% purity) and (S)-2-octylamine (S-OAm, 98% purity) were purchased from Alfa Aesar.

Characterizations

All UV-Vis spectra were recorded using an Agilent Cary 3500 spectrophotometer. Photoluminescence was recorded using a fluorescence spectrometer (FLSP920; Edinburgh Instruments, UK) equipped with an Xe lamp. Powder X-ray diffraction (XRD) patterns were tested using a Bruker D8 Advance diffractometer with graphite-monochromatized CuKα radiation ($\lambda$ = 0.15406 nm). Transmission electron microscopy (TEM) images were acquired using a JEOL JEM-3011 transmission electron microscope operated at 300 kV. High-resolution TEM images were filtered using the ABSF Filter (Average Background Subtracted Filter) implemented by Digital Micrograph. Circular dichroism spectra were measured using a JASCO CD J-815 spectrometer.

Synthesis of MBA-acetate

Acetic acid and MBA were mixed in ethanol at a molar ratio of 1.2:1. The mixture reacted in an ice bath (0 ºC) for 2 h. After completion of the reaction, the MBA-acetate was obtained by evaporation of excess acetic acid and ethanol. To ensure the purity of products, the as-prepared MBA-acetate was recrystallized thrice.

Synthesis of FA/MBA Precursor

In a three-necked round-bottomed flask, 3 mmol of FA-acetate and MBA-acetate in different ratios (MBA/FA = 0, 3%, 6%, 9%, and 12%), 3 mL of oleic acid, and 3 mL of 1-octadecene were degassed under vacuum at room temperature and 50 °C, respectively, for 30 min. The temperature was then increased to 120 °C under $N_2$ and kept at this temperature for 15 min.

Synthesis of formamidinium lead bromide ($FAPbBr_3$) nanocrystals

In a three-necked round-bottomed flask, 0.148 mmol (54.4 mg) of $PbBr_2$ and 5 mL of 1-octadecene were degassed under vacuum at room temperature and 120 °C, respectively, for 30 min. Mixtures of 2.42 mmol (0.8 mL) oleic acid, 0.9075 mmol oleylamine, and 0.3025 mmol R/S-OAm were preheated to 120 °C and then injected into the $PbBr_2$ mixture under vacuum. After $PbBr_2$ was fully dissolved, the solution became clear. The temperature of the solution was then reduced to 80 °C to prevent the rapid growth of $FAPbBr_3$ crystals. Under $N_2$ flow, 1 mL of FA/MBA precursor was swiftly injected into the $PbBr_2$ mixture, which was then quenched by immersing the flask in an ice bath after 5 s. After cooling to room temperature, the solution was centrifuged at 7000 rpm for 6 min to remove unreacted ligands and 1-octadecene. The precipitate was dispersed in 3 mL of hexane and then centrifuged at 7000 rpm for 5 min to remove precipitated particles. The solution containing $FAPbBr_3$ nanocrystals in the supernatant was placed in a refrigerator under a $N_2$ atmosphere for storage.

Solid-state NMR spectroscopy

Measurements are performed using a 600 MHz spectrometer. Samples are packed into a 1.9 mM rotor and spun at 35 kHz MAS. For each $^1H$ one-pulse measurement, 128 scans were performed and 80 kHz hard pulses were used.

Circularly polarized pump-probe transient absorption spectroscopy

Circularly polarized pump-probe transient absorption measurements were carried out using a Helios setup. Transient dynamics in the fs-ns time region (50 fs to 7 ns) was acquired with Helios in a nondegenerate pump–probe configuration. Pump pulses were generated by an optical parametric amplifier (OPerA Solo) pumped by a 1-kHz regenerative amplifier (Coherent Legend, 800 nm, 150 fs, 4 mJ). A mode-locked Ti-sapphire oscillator (Coherent Vitesse, 100 fs, 80 MHz) was used to seed the amplifier. For the 800 nm pump, the laser of the regenerative amplifier was directly used. The probe pulse was a white light continuum generated by passing the 800 nm fs pulse for the UV part (320-650 nm) through a 2 mm sapphire plate. The measurement was performed in transmission mode. Linear polarizers together with achromatic quarter-wave plates ($\lambda/4$) were used to generate circular polarization of the beams.

X-ray-triggered photopolymerization

In a typical experiment, a 50 μL hexane solution containing chiral perovskite nanocrystals (20 mg/mL) was mixed with 1 mL of diacetylene monomer (10 mg/mL in hexane). Then the mixed solution was spun onto a quartz substrate (pre-treated with UV-Ozone). The hybrid films were kept in the dark, and the hexane evaporated after a few minutes before being irradiated with X-rays. The intensity of the X-rays was set at 4 W. Various barriers can be put directly on

the top of the hybrid films. After photopolymerization, the polymer films were subjected to CD spectroscopy. Measurements were carried out by rotating the samples around the normal of the film to exclude linear dichroism and/or linear birefringence effects[4,5].

First-principles calculations

DFT-based calculations were performed using the Vienna *ab initio* simulation package with the projector-augmented wave method[1,2]. The Perdew–Burke–Ernzerh generalized gradient approximation was employed to describe the exchange-correlation interactions between electrons[3]. The kinetic energy cut off the plane wave, energy convergence criterion, and maximum remaining force on each relaxed atom were set to 520 eV, $1 \times 10^{-5}$, and 0.02 eV/Å, respectively.

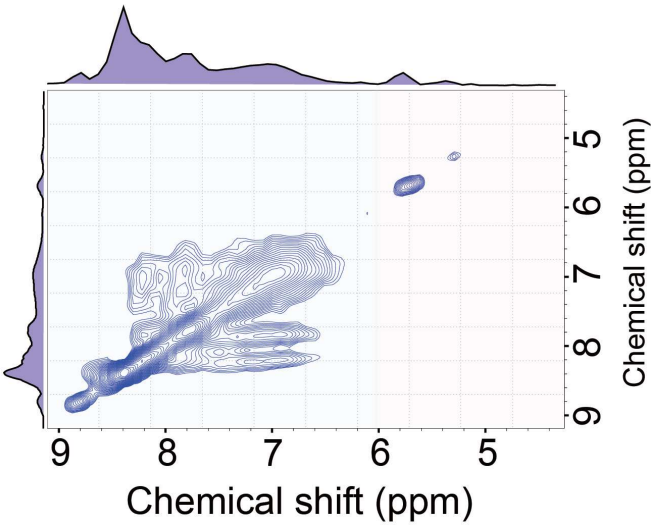


**Figure S1.** Two-dimensional solid-state NMR spectra of reference $FAPbBr_3$ perovskite nanocrystals.

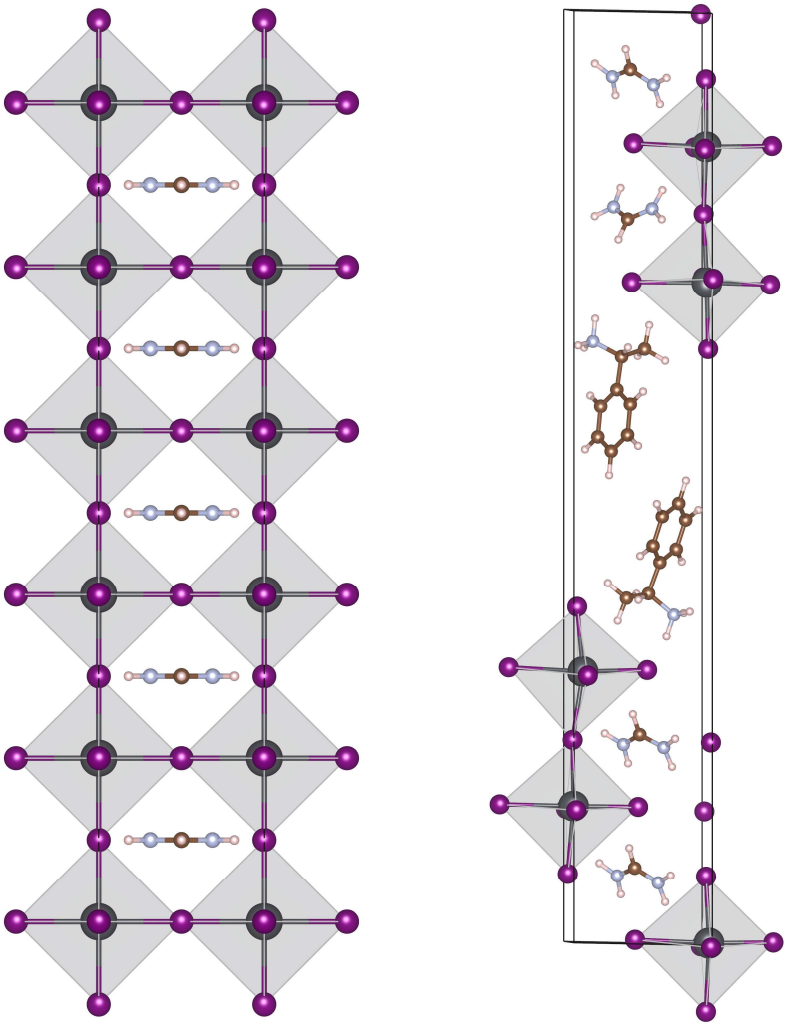

**Figure S2.** DFT-optimized $FAPbBr_3$ (left panel) and MBA-doped $FAPbBr_3$ (right panel) 1 × 1 × 5 supercells. Purple, silver, brown, gray, and white balls denote bromide, lead, carbon, nitrogen, and hydrogen atoms, respectively.

**Table S1.** Lattice parameters of DFT-optimized $FAPbBr_3$ and MBA-doped 1 × 1 × 5 supercells

| Sample | a (Å) | b (Å) | c (Å) | α (degree) | β (degree) | γ (degree) |
|---|---|---|---|---|---|---|
| $FAPbBr_3$ | 6.224 | 5.988 | 30.919 | 90.000 | 90.000 | 90.000 |
| MBA-doped $FAPbBr_3$ | 6.266 | 6.139 | 42.22 | 89.407 | 88.897 | 85.662 |

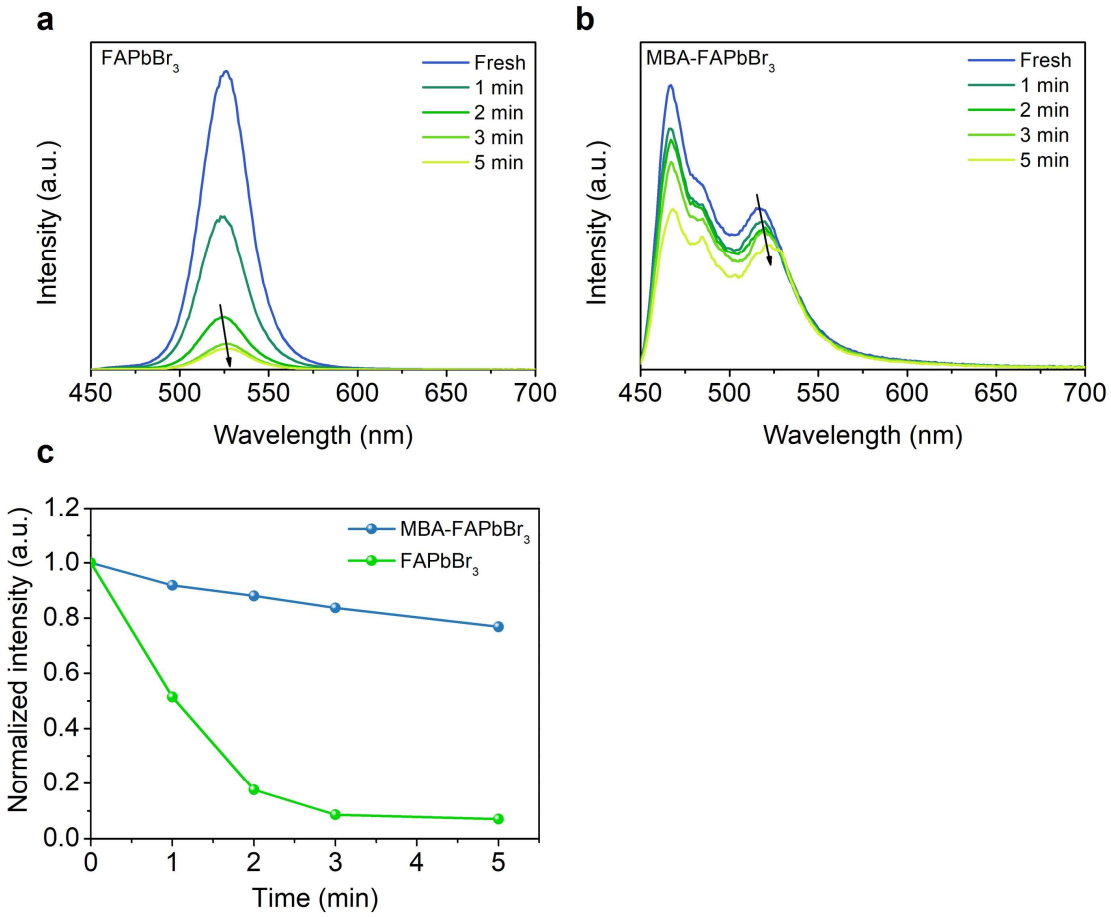


**Figure S3.** (**a** and **b**) Photoluminescence (PL) spectra of 3D $FAPbBr_3$ and MBA-doped $FAPbBr_3$ nanocrystals, respectively, exposed to 85 ºC in an ambient atmosphere for varying durations. **(c)** PL intensity of $FAPbBr_3$ and MBA-doped $FAPbBr_3$ nanocrystals over time. Notably, the thermal stability of perovskite nanocrystals was investigated by comparing the PL intensity between MBA-doped $FAPbBr_3$ and 3D $FAPbBr_3$ nanocrystals at 85 ºC in an ambient atmosphere. After 5 min of heating at 85 ºC, the PL intensity of 3D $FAPbBr_3$ decreased from 100% to 7%, while MBA-doped $FAPbBr_3$ nanocrystals maintained 76.8% of their original intensity, demonstrating the enhanced thermal stability of MBA-doped $FAPbBr_3$ over 3D $FAPbBr_3$ nanocrystals.

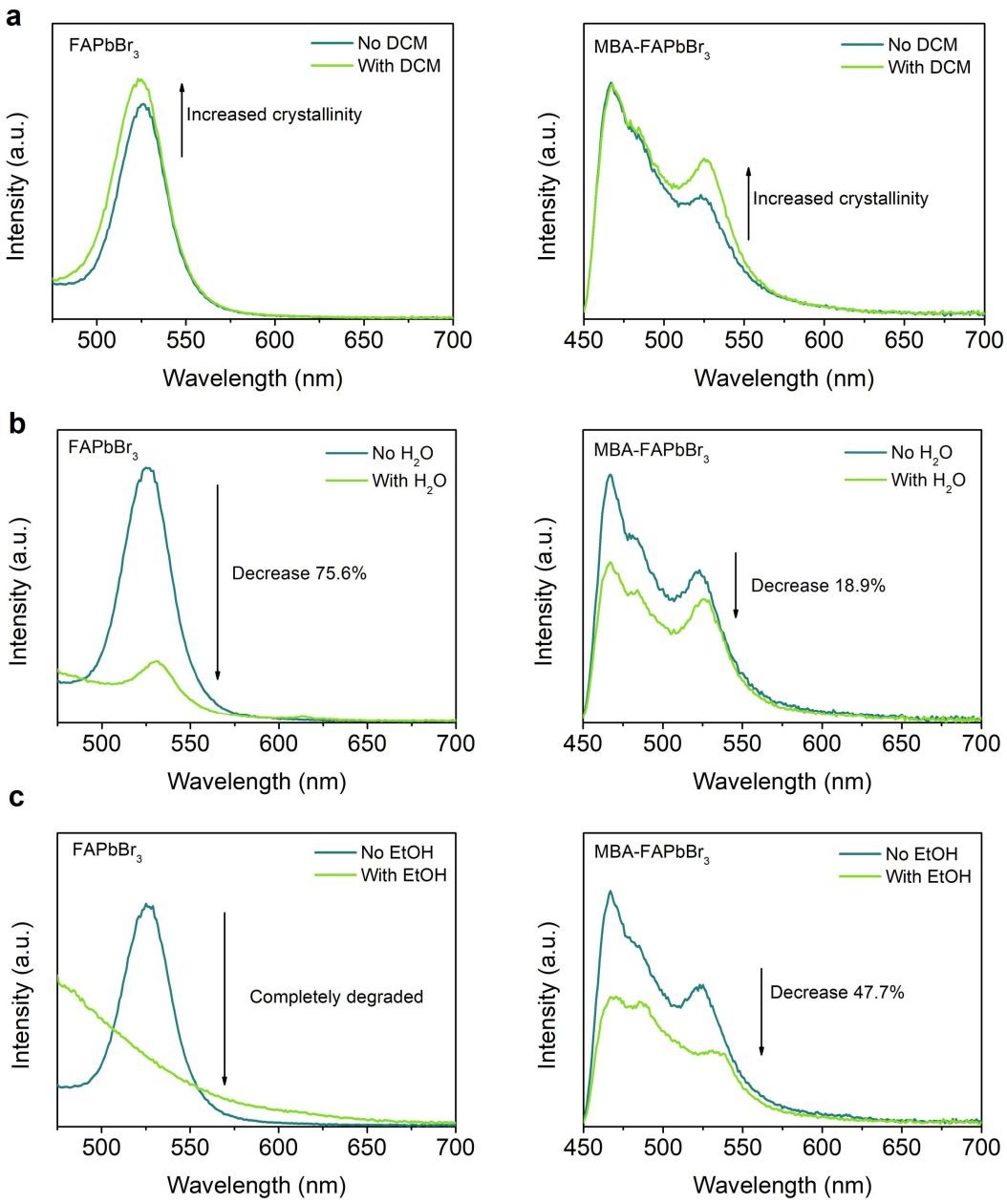


**Figure S4.** Photoluminescence (PL) spectra recorded for 3D $FAPbBr_3$ and MBA-doped $FAPbBr_3$ nanocrystals with and without **(a)** dichloromethane (DCM) in the solvent mixture (200 µL nanocrystals in hexane with 40 µL DCM), **(b)** water ($H_2O$) in the solvent mixture (200 µL nanocrystals in hexane with 20 µL $H_2O$), and **(c)** ethanol in the solvent mixture (EtOH) (200 µL nanocrystals in hexane with 400 µL EtOH). The chemical stability of the nanocrystals was evaluated by comparing the PL intensity after immersion in different solvents. The introduction of DCM enhanced the PL intensity of both 3D $FAPbBr_3$ and MBA-doped $FAPbBr_3$ nanocrystals due to its ability to improve perovskite crystallinity. In contrast, the PL intensity of 3D $FAPbBr_3$ nanocrystals significantly decreased by 75.6% in $H_2O$ and was completely quenched in EtOH. However, MBA-doped $FAPbBr_3$ nanocrystals showed only a modest reduction of 18.9% in $H_2O$ and 47.7% in EtOH, highlighting their enhanced chemical stability over 3D $FAPbBr_3$ nanocrystals.

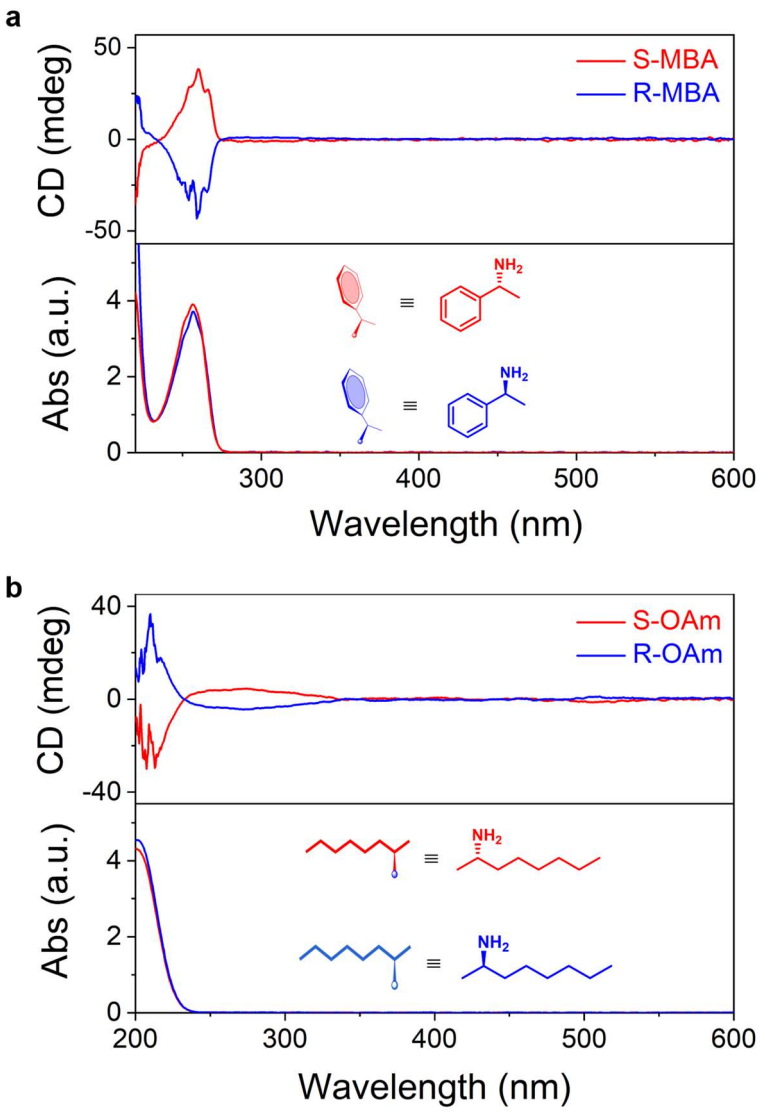


**Figure S5.** CD and UV-Vis spectra of **(a)** MBA and **(b)** OAm molecules.

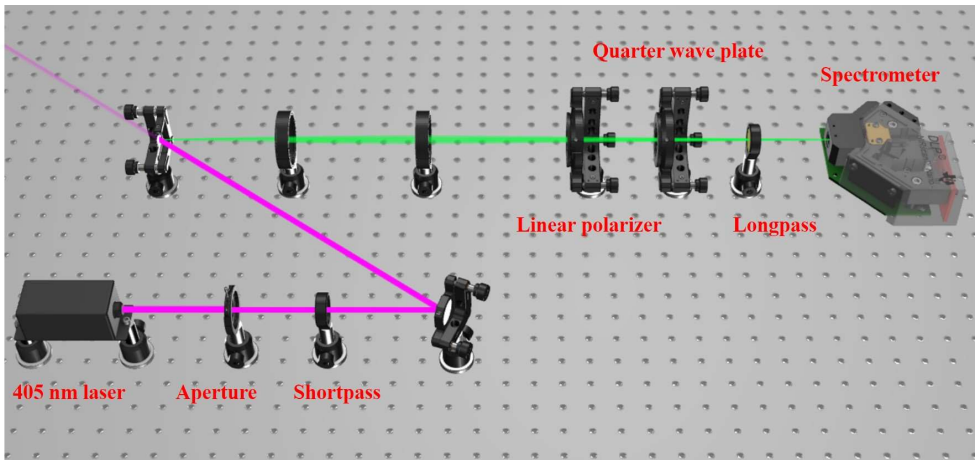


**Figure S6.** Optical setup for the polarization-resolved photoluminescence spectroscopy. The main optical components include a linear polarizer, a quarter-wave plate, and a longpass filter.

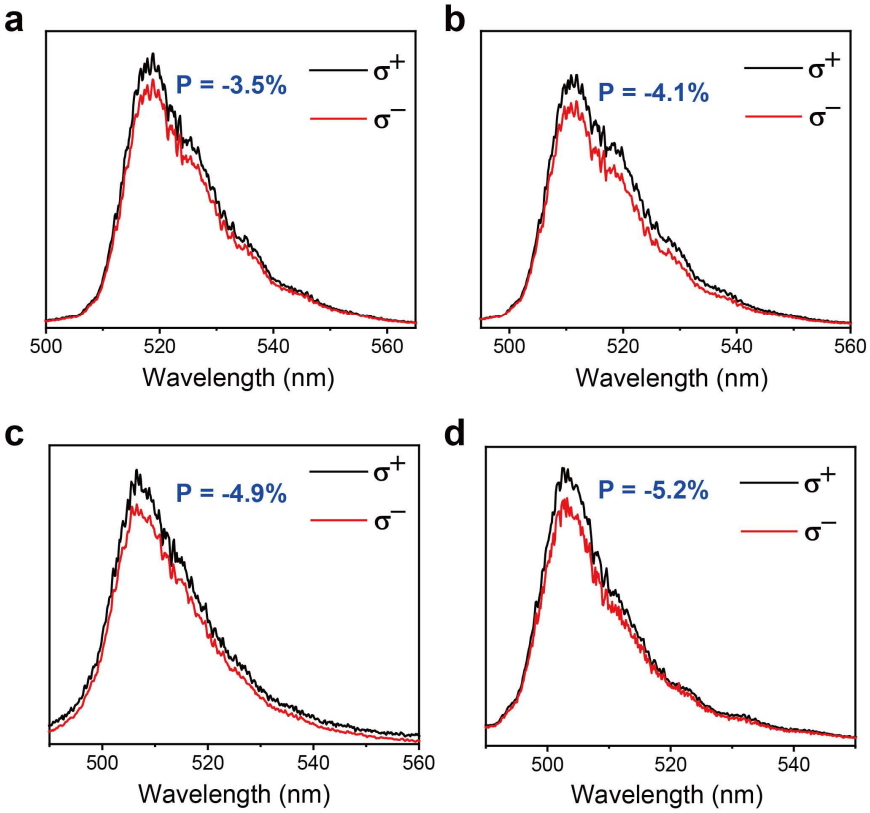


**Figure S7.** Polarization-resolved photoluminescence spectra of SS perovskite nanocrystals with **(a)** 3%, **(b)** 6%, **(c)** 9%, and **(d)** 12% S-MBA in the crystal structure ($\lambda_{ex}$ = 405 nm).

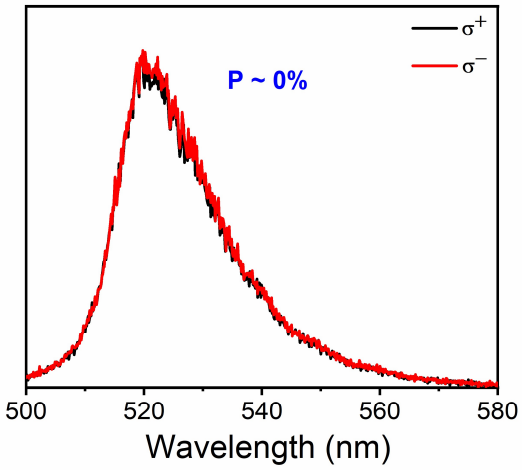


**Figure S8.** Polarization-resolved photoluminescence spectra of perovskite nanocrystals functionalized exclusively with R-MBA within the crystal structure. These measurements were conducted at room temperature ($\lambda_{ex}$ = 405 nm).

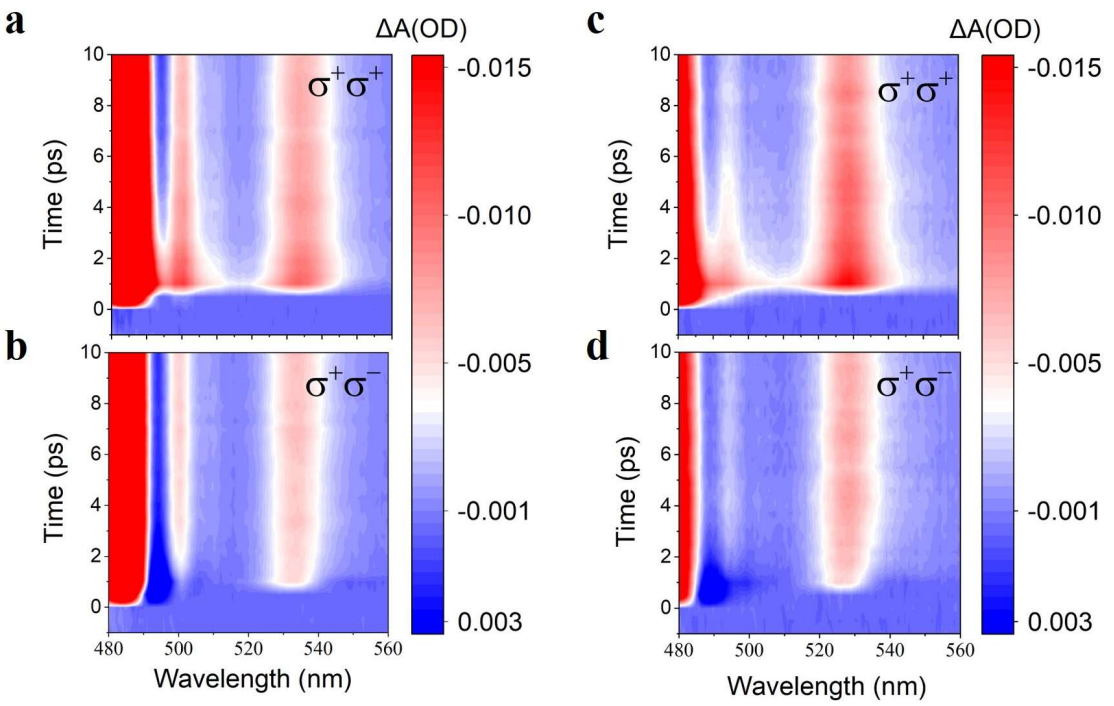


**Figure S9.** Circularly polarized pump-probe transient absorption (CP-TA) spectra of RR and RS perovskite nanocrystals with 475 nm excitation. For RR perovskite nanocrystals, by applying **(a)** a right-handed circularly polarized pump with a right-handed circularly polarized probe ($\sigma^+\sigma^+$) and **(b)** a right-handed circularly polarized pump with a left-handed circularly polarized probe ($\sigma^+\sigma^-$). For RS perovskite nanocrystals, by applying **(c)** a right-handed circularly polarized pump with a right-handed circularly polarized probe ($\sigma^+\sigma^+$) and **(d)** a right-handed circularly polarized pump with a left-handed circularly polarized probe ($\sigma^+\sigma^-$).

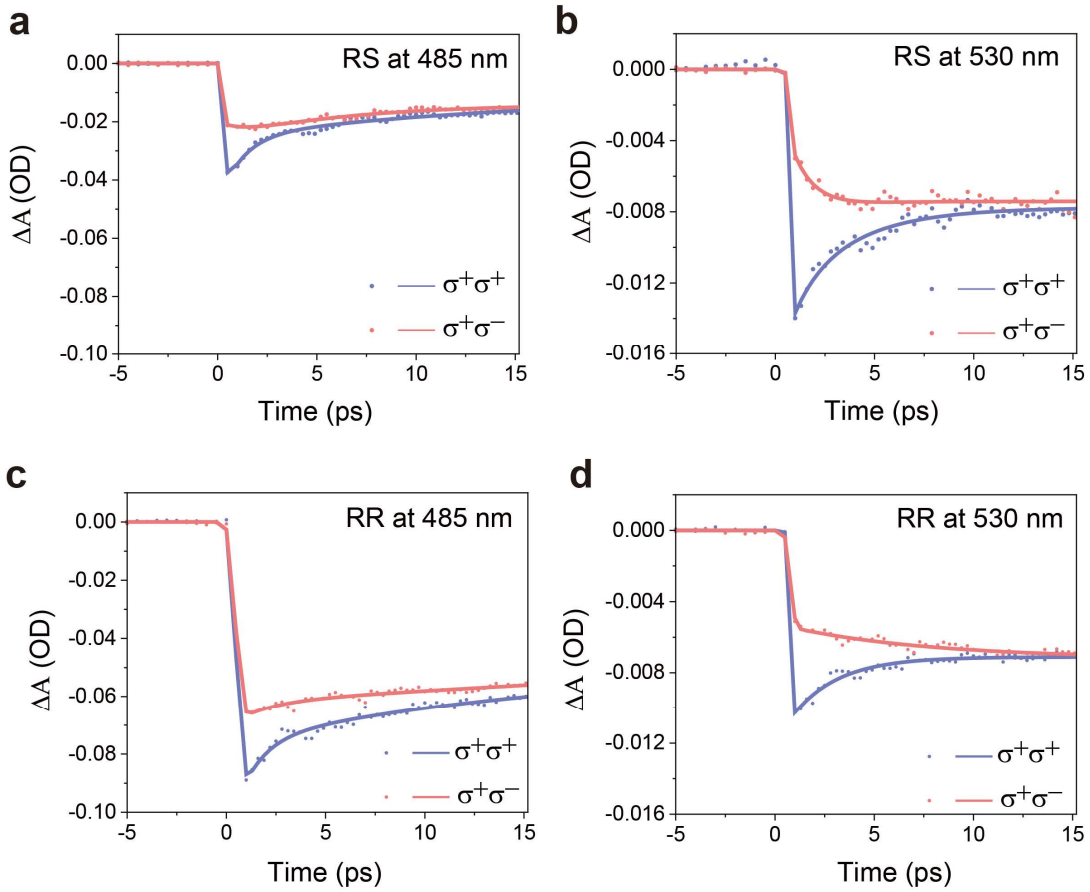


**Figure S10.** Spin-resolved kinetic curves for RS perovskite nanocrystals at **(a)** 485 nm and **(b)** 530 nm, and for RR perovskite nanocrystals at **(c)** 485 nm and **(d)** 530 nm. All data show the kinetic process within the first 15 ps. The excitation light employed is a femtosecond pulsed laser with a wavelength of 475 nm and a repetition rate of 1 kHz, generated by an optical parametric amplifier. The polarization states of the two beams are modulated using a combination of a linear polarizer and a quarter-wave plate.

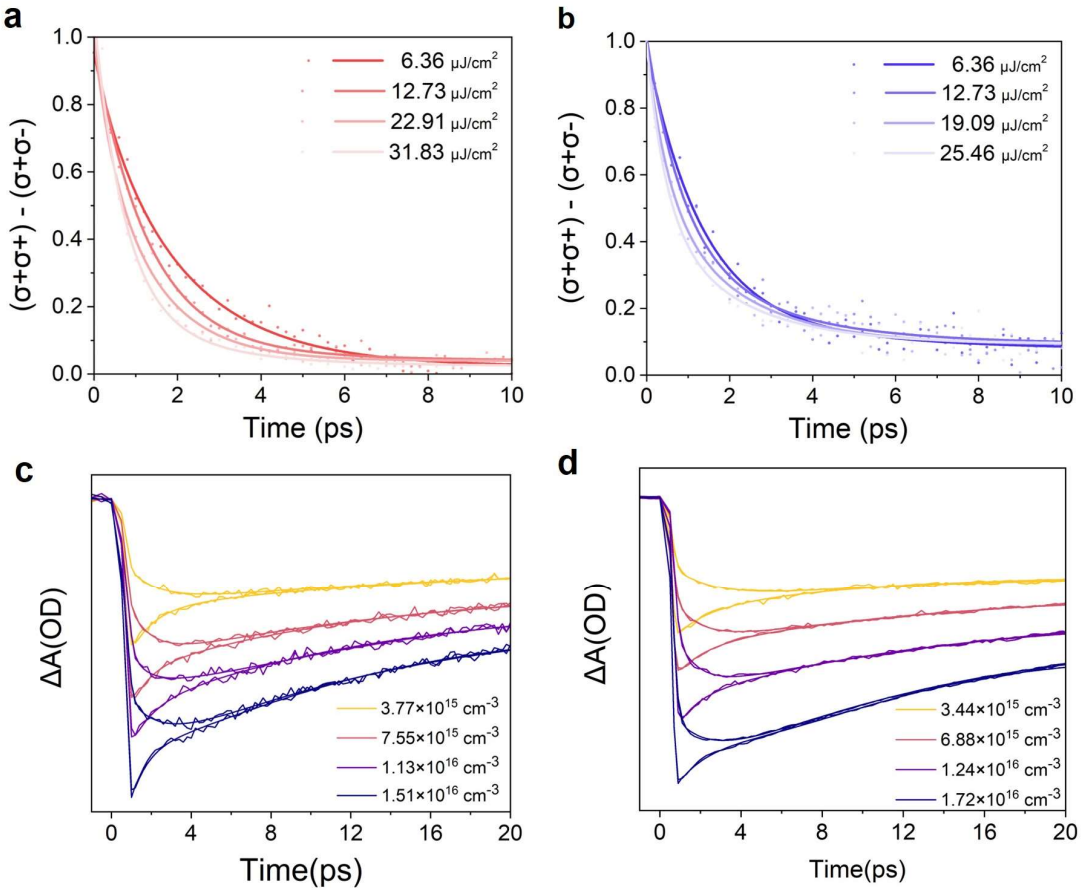


**Figure S11.** Power-dependent spin relaxation dynamics of nanocrystals modified with **(a)** chiral and **(b)** achiral OAm ligands. Circularly polarized transient absorption dynamics in perovskite nanocrystals modified with **(c)** chiral and **(d)** achiral OAm ligands at different excitation carrier densities.

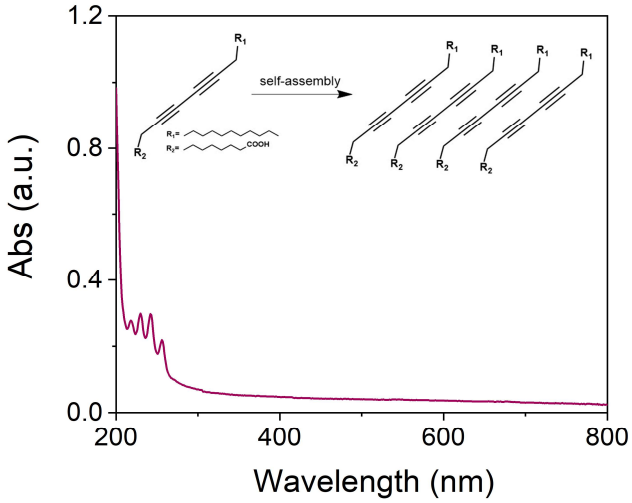


**Figure S12.** UV-Vis spectrum of diacetylene monomers. Inset shows the chemical formula and self-assembly behavior of the diacetylene monomer in the solid state.

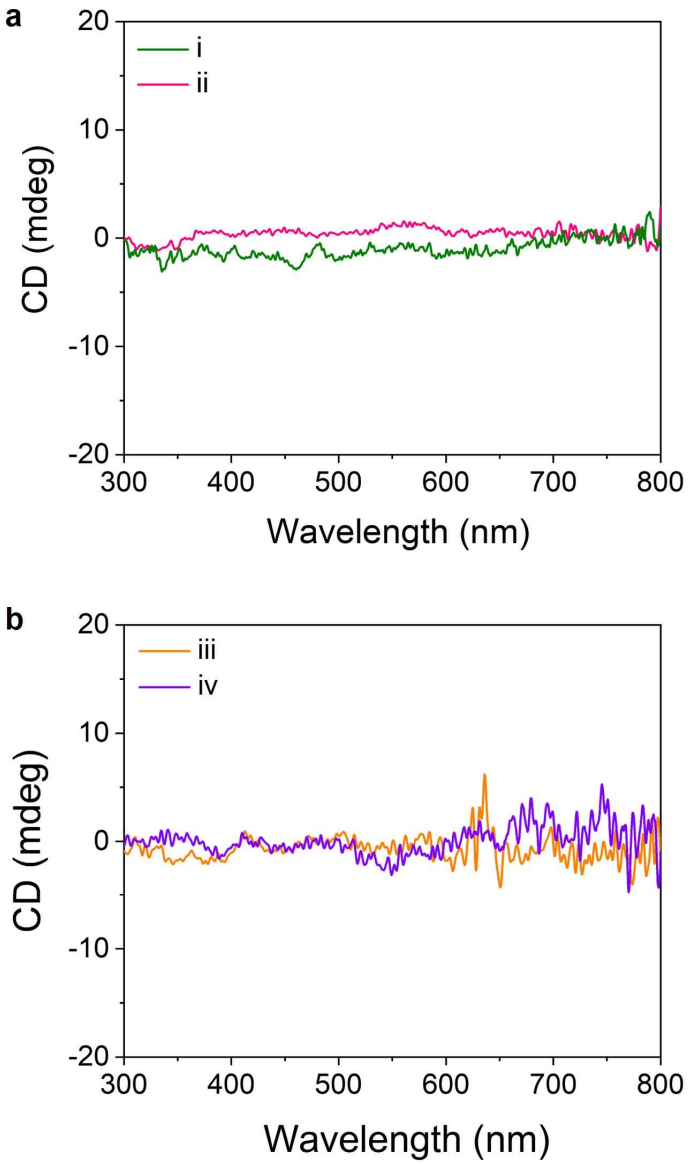


**Figure S13. (a)** CD spectra of polydiacetylene films induced by (i) RS nanocrystals and (ii) SR perovskite nanocrystals under X-ray irradiation at room temperature. **(b)** CD spectra of polydiacetylene films induced by (iii) R-MAB and (iv) R-OAm under X-ray irradiation at room temperature.

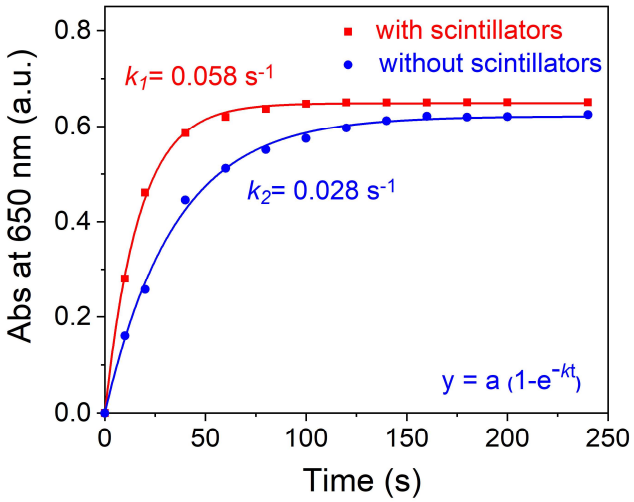


**Figure S14.** Time evolution of the maximum absorption at 650 nm for polydiacetylene polymerized with/without the assistance of perovskite scintillators under the same condition of X-ray. The photopolymerization of monomers is described as a first-order reaction, which can be determined as $\ln [(A_\infty - A_t)/(A_\infty - A_0)] = -kt$, where $A_0$, $A_t$, and $A_\infty$ are ascribed as the absorbance at the initial time, the present time t and the stationary state, while $k$ is the photopolymerization rate constant and t is the irradiation time. By empirical fitting, the polymerization rate constant $k$ for monomers film (without scintillators) and hybrid film (with scintillators) were estimated to be 0.028 $s^{-1}$ and 0.058 $s^{-1}$, respectively. The reaction rate in the hybrid film was about two-times faster than that in pure monomers film.

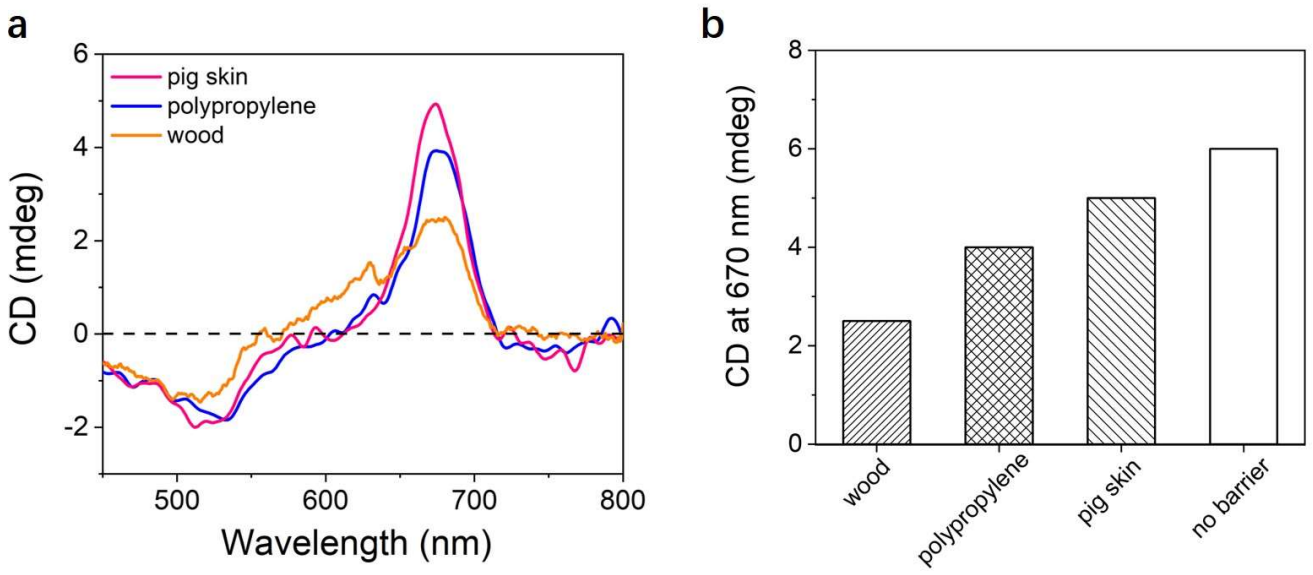


**Figure 15**. (a) CD spectra depicting the response of polydiacetylene induced by SS nanocrystals under X-ray irradiation while penetrating wood, polypropylene film and pig skin tissue. (b) Summary of CD intensity at ~670 nm revealing the behavior of polydiacetylene induced by SS nanocrystals under X-ray irradiation when penetrating wood, polypropylene film, pig skin tissue, and in the absence of any barrier (control).

**References**


1 Kresse, G., and Furthmüller, J. (1996). Efficiency of ab-initio total energy calculations for metals and semiconductors using a plane-wave basis set. Comput. Mater. Sci. *6*, 15.

2 Blöchl, P. E. (1994). Projector augmented-wave method. Phys. Rev. B *50*, 17953.

3 Perdew, J.P., Burke, K., and Ernzerhof, M. (1996). Generalized gradient approximation made simple. Phys. Rev. Lett. *77*, 3865.

4 Albano, G., Pescitelli, G., amd Di Bari, L. (2020). Chiroptical properties in thin films of π-conjugated systems. Chem. Rev. *120*, 10145.

5 He C, Yang G, Kuai Y, et al. (2018) Dissymmetry enhancement in enantioselective synthesis of helical polydiacetylene by application of superchiral light. Nat. Commun., *9*, 5117.